Chemical Science

ROYAL SOCIETY OF CHEMISTRY

EDGE ARTICLE

View Article Online
View Journal | View Issue

Cite this: *Chem. Sci.*, 2020, **11**, 8617

All publication charges for this article have been paid for by the Royal Society of Chemistry

Construction of coacervate-in-coacervate multi-compartment protocells for spatial organization of enzymatic reactions†

Yufeng Chen, Min Yuan, Yanwen Zhang, Songyang Liu, Xiaohai Yang, Kemin Wang * and Jianbo Liu *

Received 14th July 2020
Accepted 30th July 2020

DOI: 10.1039/d0sc03849k

rsc.li/chemical-science

Coacervate microdroplets, formed *via* liquid–liquid phase separation, have been extensively explored as a compartment model for the construction of artificial cells or organelles. In this study, coacervate-in-coacervate multi-compartment protocells were constructed using four polyelectrolytes, in which carboxymethyl-dextran and diethylaminoethyl-dextran were deposited on the surface of as-prepared polydiallyldimethyl ammonium/deoxyribonucleic acid coacervate microdroplets through layer-by-layer assembly. The resulting multi-compartment protocells were composed from two immiscible coacervate phases with distinct physical and chemical properties. Molecule transport experiments indicated that small molecules could diffuse between two coacervate phases and that macromolecular enzymes could be retained. Furthermore, a competitive cascade enzymatic reaction of glucose oxidase/horseradish peroxidase–catalase was performed in the multi-compartment protocells. The different enzyme organization and productions of H_2O_2 led to a distinct polymerization of dopamine. The spatial organization of different enzymes in immiscible coacervate phases, the distinct reaction fluxes between coacervate phases, and the enzymatic cascade network led to distinguishable signal generation and product outputs. The development of this multi-compartment structure could pave the way toward the spatial organization of multi-enzyme cascades and provide new ideas for the design of organelle-containing artificial cells.

Introduction

Currently, coacervate microdroplets as a powerful means of compartmentalization have been extensively explored as a compartment model for the construction of artificial protocells and organelles.[1,2] Complex coacervation is an associative, liquid–liquid phase separation phenomenon driven by an initial electrostatic attraction between oppositely charged polyelectrolytes.[3] Based on their high sequestration capability[4] and macromolecular crowded interior,[5] a range of protocellular functionalities have been demonstrated in the biomimetic models, including *in vitro* gene expression,[6] enhanced enzyme and RNA catalysis,[7] and chemical signaling.[8] Interestingly, the formation of membrane-free compartments or condensates such as P-bodies,[9] stress granules,[10] and Cajal bodies[11] within cells has also been associated with the liquid–liquid phase separation of coacervation.[12] These intracellular membrane-free organelles are chemically isolated from their surrounding cytoplasm *via* a diffusive phase boundary.[12] The importance of coacervates as artificial compartment models, combined with their relevance in biology, has inspired us to explore the construction of well-defined high-grade coacervates with complex micro-architectures.

The construction of multi-compartment micro-architectures, in which sub-compartments reside in larger ones, has gained current much attention.[13–15] A multi-compartment structure can perform distinct biochemical reactions in one pot, just as in living cellular systems, which not only enables the positional assembly and spatial separation of biomolecules and reactions in different domains,[16] but also could allow for spatially segregated reactions or incompatible components to run simultaneously inside host compartments.[17,18] A wide variety of multi-compartment structures have been used to create by using layer-by-layer self-assembly, Pickering emulsion method and microfluidic chip[19,20] for chemical signal communication,[21] sustained delivery of drug[22] and mimic the behavior of cell.[23] As of now, different types of soft components, including liposomes,[24] polymersomes,[25] polymer capsules,[26] and coacervates,[27,28] have been integrated for the fabrication of multi-compartment systems within nested constructs such as vesosome,[29–31] capsosome,[32–35] polymersome-in-polymersome,[36,37] and polymersome-in-hydrogel[38] micro-architectures. There have been a few

State Key Laboratory of Chemo/Biosensing and Chemometrics, College of Chemistry and Chemical Engineering, Key Laboratory for Bio-Nanotechnology and Molecular Engineering of Hunan Province, Hunan University, Changsha 410082, P. R. China. E-mail: liujianbo@hnu.edu.cn; kmwang@hnu.edu.cn

† Electronic supplementary information (ESI) available: Zeta size, optical images, enzyme activities, *etc.* See DOI: 10.1039/d0sc03849k

reports on the construction of coacervate-based heterozygous multi-compartments, including coacervates-in-liposomes,[39–42] coacervate-in-polymersome,[43] and vesicle-in-coacervate.[44] However, to the best of our knowledge, no study has examined the construction of coacervate-in-coacervate structures from the perspective of multi-compartment protocells. One example of an intracellular coacervate-in-coacervate structure is the nucleolus, *i.e.*, the largest nuclear body, which exhibits a core–shell architecture thought to be important for the sequential processing of nascent rRNA transcripts.[45]

In this study, a coacervate-in-coacervate multi-compartment micro-architecture is designed and constructed *via* a bottom-up layer-by-layer assembly method. Our design involves four polyelectrolyte components, *i.e.*, polydiallyldimethyl ammonium (PDDA), deoxyribonucleic acid (DNA), diethylaminoethyl-dextran (DEAE-dextran), and carboxymethyl-dextran (CM-dextran). In detail, the inner sub-compartment is formed by liquid–liquid phase separation of strong polyelectrolytes PDDA/DNA. Then, CM-dextran and DEAE-dextran are deposited on the surface of as-prepared PDDA/DNA compartments through layer-by-layer assembly (Fig. 1A). Subsequently, a competitive cascade enzymatic reaction of glucose oxidase (GOx)/horseradish peroxidase (HRP)–catalase (CAT) is performed to demonstrate the functionalities of the multi-compartment micro-architecture. Three enzymes are simultaneously immobilized in the inner coacervate microdroplets (Fig. 1B, Case I), and GOx/HRP and CAT are immobilized in the inner and outer coacervate microdroplets, respectively (Fig. 1C, Case II). The glucose-mediated fluorescence production is investigated in these two cases. The different spatial organization of the cascade enzymes and distinct reaction fluxes between the coacervate phases lead to distinguishable signal generation and product outputs. In this way, a spatially segregated enzyme immobilization and enzymatic cascade network are created in this artificial coacervate-in-coacervate multi-compartment protocell.

Results and discussion

Preparation of coacervate-in-coacervate multi-compartment microdroplets

The coacervate-in-coacervate microdroplets were constructed through layer-by-layer technology, in which CM-dextran and DEAE-dextran polyelectrolytes were serially assembled on the surface of an as-prepared PDDA/DNA coacervate phase. To start, the preparation and characterization of the PDDA/DNA coacervate microdroplets were systematically investigated. The aqueous dispersion of the PDDA/DNA coacervate microdroplets was obtained by directly mixing a PDDA solution (average M_w 20–35 w, pH = 8.0) and DNA solution (low molecular weight from salmon sperm, pH = 8.0) at different weight ratios (0.1–0.7). A partial phase diagram was plotted through the transmittance determination of the coacervate suspension at 360 nm and illustrated a concentration-dependent contour line (Fig. 2A). An increase of the polyelectrolyte facilitated the formation of concentrated coacervate microdroplets with a very low transmittance. Zeta potential measurements of the coacervate microdroplets showed that their zeta potentials changed from negative to positive in the range from −38.4 mV to

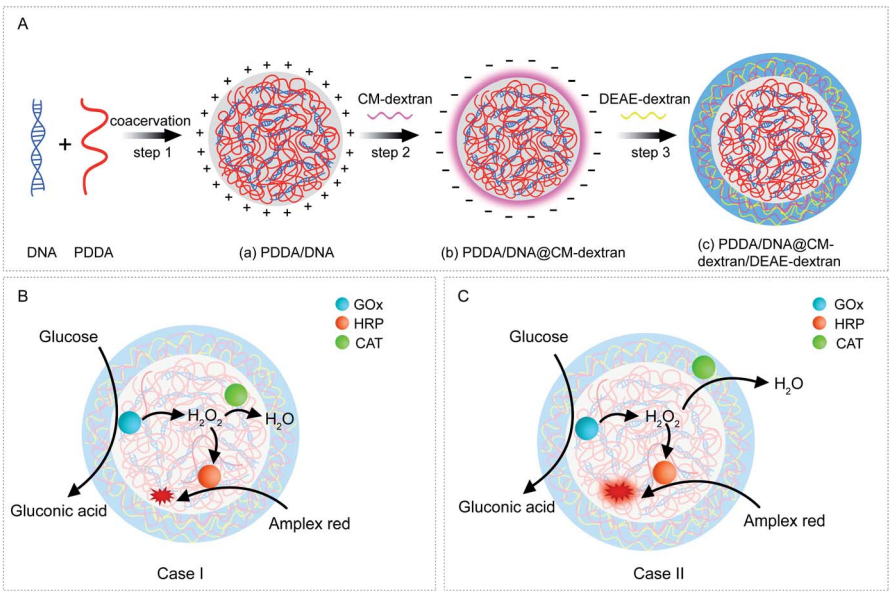

Fig. 1 (A) Schematic illustration of the coacervate-in-coacervate synthetic procedure *via* a layer-by-layer assembly method. Step 1: PDDA/DNA coacervate microdroplets were synthesized through electrostatic assembly of PDDA and DNA polyelectrolytes. Step 2: PDDA/DNA@CM-dextran coacervate microdroplets were formed by the assembly of CM-dextran on positively charged PDDA/DNA coacervates. Step 3: PDDA/DNA@CM-dextran/DEAE-dextran coacervates were formed by the assembly of DEAE-dextran on negatively charged PDDA/DNA@CM-dextran coacervates. (B, C) Schematic representation of the spatial organization of the coacervate-in-coacervate enzymatic cascade. The GOx, HRP, and CAT enzymes could be immobilized in the multi-compartment microdroplets through synchronous assembly. (B) Case I: GOx/HRP and CAT were all encapsulated in the inner compartments of the coacervates. (C) Case II: GOx/HRP and CAT were separately encapsulated in the inner and outer compartments of the coacervates, respectively.

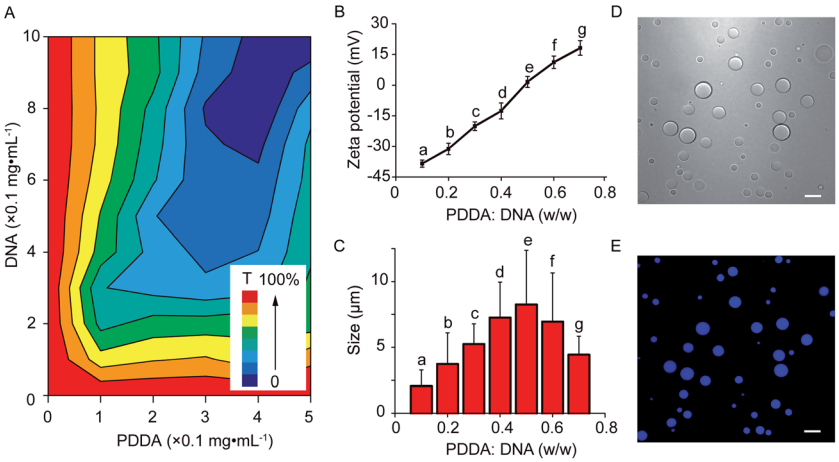

Fig. 2 Preparation of PDDA/DNA coacervate microdroplets. (A) Partial phase diagram for the PDDA/DNA coacervate microdroplet plot from the transmittance (T) measurements at different concentrations (PDDA : DNA in weight) of the polyelectrolyte pair. (B, C) (B) The zeta potential and (C) size measurement at different weight ratios of the PDDA/DNA coacervates. (D, E) Confocal images of the coacervates; bright field (D) and fluorescent field (E) imaging of the PDDA/DNA coacervates (PDDA : DNA = 0.5 in weight), respectively. The coacervates were stained with Hoechst. Scale bar: 10 μm.

+18.1 mV after the weight ratio gradually increased from 0.1 to 0.7 (PDDA : DNA in weight) (Fig. 2B). The hydrodynamic diameters of the coacervate microdroplets initially increased and then decreased as the weight ratios increased, as determined by dynamic light scattering (Fig. 2C). The near stoichiometric charge neutralization of the polyelectrolyte complex (spot e, PDDA : DNA = 0.5 in weight) generated a large turbidity dispersion containing large spherical microdroplets with a mean size of 8.0 ± 5.0 μm (Fig. 2C). In our system, mixing the PDDA and DNA solutions at the weight ratio of 0.6 ([coacervate] = 1 mg mL^{-1}) resulted in the formation of positive coacervate microdroplets with a zeta potential of 11.1 mV and a transmittance of 17.6% (spot f, PDDA : DNA = 0.6 in weight). The bright images of the coacervates showed discrete spherical droplets. The prepared coacervate microdroplets were stained with DNA-binding fluorescent Hoechst dye for fluorescent imaging and exhibited homogeneous blue fluorescence with high contrast (Fig. 2D and E). The as-prepared positively charged PDDA/DNA coacervates could serve as inner microdroplets for the layer-by-layer growth of outer coacervates, in which negatively charged CM-dextran and positively charged DEAE-dextran polyelectrolytes were serially added. Positively charged PDDA/DNA coacervates (ζ = +11.1 ± 0.9 mV, d = 5.5 ± 1.3 μm) at the weight ratio of 0.6 (PDDA : DNA) were utilized for the assembly of the coacervate-in-coacervate microdroplets (Fig. 3A–C, (a)). The addition of the CM-dextran solution into the above coacervate suspension with an optimized ratio of CM-dextran : PDDA/DNA = 3 in weight led to

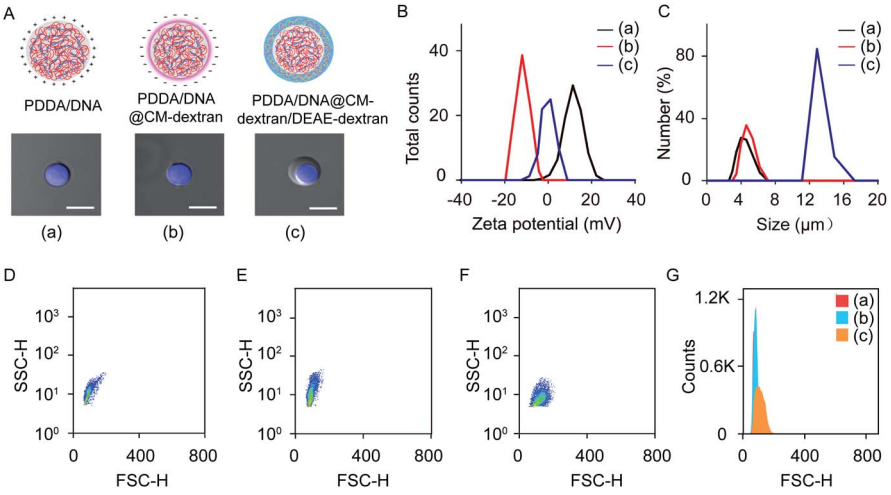

Fig. 3 Preparation of the coacervate-in-coacervate microdroplets. (A) Illustration and optical imaging of the PDDA/DNA coacervates (a), PDDA/DNA@CM-dextran coacervates (b), and PDDA/DNA@CM-dextran/DEAE-dextran coacervates (c). Scale bar: 10 μm. (B, C) The zeta potentials (B) and hydrodynamic sizes (C) of three different coacervates. (D–G) Flow cytometry of FSC/SSC 2D dot plots. (D–F) Different coacervates prepared at different steps: PDDA/DNA (D), PDDA/DNA@CM-dextran (E), and PDDA/DNA@CM-dextran/DEAE-dextran coacervates (F). (G) The histogram of the HSC signal as determined from the 2D dot plots.

a negligible change in the hydrodynamic sizes (5.7 ± 1.2 μm) but reversed the zeta potentials of the PDDA/DNA coacervate microdroplets to −12.6 mV (Fig. 3A–C, (b) and S1A†). Optical images showed no obvious changes in the morphology of the resultant PDDA/DNA@CM-dextran microdroplets in comparison with the PDDA/DNA microdroplets (Fig. 3A). Subsequently, the DEAE-dextran solution was added to the PDDA/DNA@CM-dextran microdroplets with a ratio of DEAE-dextran : PDDA/DNA@CM-dextran = 0.3 in weight, which initiated a nucleation of the CM-dextran/DEAE-dextran surrounding the PDDA/DNA@CM-dextran coacervate as well as the formation of a coacervate-in-coacervate microdroplet with a double-compartment structure. This process facilitated a size increase of the microdroplets (12.7 μm) and a restoration of the zeta potential from negative to positive (1.3 mV) (Fig. 3A–C, (c) and S1B†). The above results could serve as proof that a coacervate-in-coacervate structure was successfully generated *via* two-step layer-by-layer self-assembly. In the process of constructing of coacervate-in-coacervate structure, the formation efficiency of coacervate-in-coacervate multi-compartment was estimated to be 95.3% through a confocal imaging of numerous protocells (Fig. S2†).

Flow cytometry was used to statistically characterize the preparation of the multi-compartment microdroplets. Experiments using PDDA/DNA, PDDA/DNA@CM-dextran, and PDDA/DNA@CM-dextran/DEAE-dextran coacervate microdroplets all yielded two-dimensional (2D) dot plots of forward light scatter height (FSC-H) *versus* side light scatter height (SSC-H) (Fig. 3D–F). A quantitative analysis of these different coacervates was shown in Fig. 3G. Both the PDDA/DNA and PDDA/DNA@CM-dextran coacervate microdroplets demonstrated a similar scattering pattern with a narrow distribution of FSC values and a wide distribution of SSC values (Fig. 3D and E). However, the PDDA/DNA@CM-dextran/DEAE-dextran coacervate microdroplets showed an FSC signal enhancement (Fig. 3F), which provided a relative size for the microdroplets, as it is a measurement of the amount of a laser beam that passes around a target.[46] Therefore, the results did not indicate any obvious size change between the PDDA/DNA and PDDA/DNA@CM-dextran coacervate microdroplets; however, the final PDDA/DNA@CM-dextran/DEAE-dextran coacervate microdroplets demonstrated a size increase and a size distribution broadening. These results were consistent with those of the dynamic light scattering and optical imaging. The outer layer was constructed through layer-by-layer assembly of CM-dextran/DEAE-dextran. During the preparation of the compartmented microdroplets, increasing the weight ratio of CM-dextran and DEAE-dextran adjusted the size of outer compartment, even led to the formation of multi-layer compartments. For example, the weight ratio of 5 : 5 : 1 (CM-dextran : DEAE-dextran : PDDA/DNA) resulted in the formation of a three-layer multi-compartment structure (Fig. S3†).

Characterization of coacervate-in-coacervate multi-compartment microdroplets

The coacervate-in-coacervate compartments were characterized through fluorescent imaging, in which PDDA/DNA and CM-dextran/DEAE-dextran were stained with Hoechst and FITC-CAT, respectively. As illustrated in the single-microdroplet imaging, the green fluorescence in the outer layer and blue in the inner layer exhibited a high optical contrast, indicative of a double-compartment microstructure (Fig. 4A and B). Both the three-dimensional (3D) reconstruction image (Fig. 4D) and fluorescence intensity profiles (Fig. 4E) demonstrated that a large inner microdroplet with blue fluorescence was surrounded by a coacervate microsphere as an outer compartment. Interestingly, the position of the inner PDDA/DNA coacervate distributed in the outer compartment was dynamically variable. In most cases, inner coacervates are located in the inner edge of the outer coacervates. Time-dependent optical imaging showed random movement of the inner microdroplets in the host compartment (Movie S1†), which was attributed to the high liquid-like fluidity of the coacervate matrix.

In our system, the formation of the coacervate-in-coacervate structure was attributed to the different electrostatic attraction of PDDA/DNA and CM-dextran/DEAE-dextran. Due to the high charge density of PDDA and DNA polyelectrolytes, the PDDA/DNA coacervates demonstrated a high binding capability and structural stability. These qualities were confirmed *via* salt tolerance experiments, in which coacervate microdroplets were treated with different concentrations of NaCl solutions. It was determined that the threshold NaCl concentration for the destabilization of the PDDA/DNA coacervate was 0.64 M, approximately 8 times higher than that of the CM-dextran/DEAE-dextran (0.08 M) (Fig. S4†). In the coacervate-in-coacervate compartments, two different coacervate phases possessed distinguishable physical and chemical parameters concerning their density, dielectric constant (ε), and partition

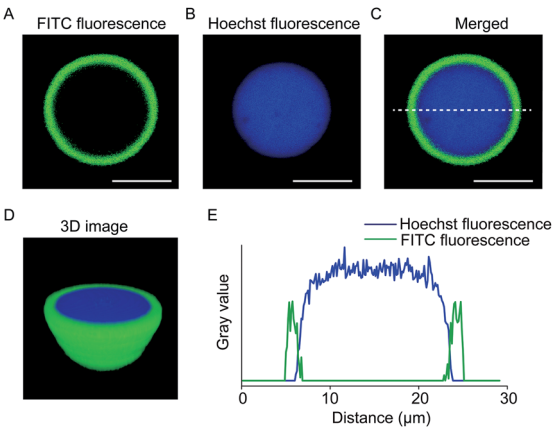

Fig. 4 Fluorescent imaging of coacervate-in-coacervate multi-compartment protocells. (A–C) Cross-sectional fluorescence images. (A) FITC green fluorescent imaging, (B) Hoechst blue fluorescent imaging, and (C) merged fluorescent image of single PDDA/DNA@CM-dextran/DEAE-dextran coacervate microdroplets. The inner and outer layers of the coacervate-in-coacervate microdroplets were encapsulated with Hoechst (blue fluorescence) and FITC-CAT (green fluorescence), respectively. (D) 3D confocal image of the coacervate-in-coacervate structure. (E) The corresponding fluorescence intensity profile of the green and blue fluorescence intensity across the coacervate-in-coacervate microstructure from (C). Scale bar: 10 μm.

coefficient (Table S1 and Fig. S5†). The partition coefficient (K) of methylene blue in the PDDA/DNA and DEAE-dextran/CM-dextran was determined to be 169 and 3.8 (Fig. S6†), respectively. The large partition coefficient for the PDDA/DNA coacervate indicated that small molecular such as the dyes would be sequestrated into the inner compartment. In the separated coacervate compartments, small molecules could diffuse between the different coacervate compartments. For example, after fluorescein was added into the coacervate suspension, a fluorescence enhancement was observed in the inner PDDA/DNA coacervate, indicating the diffusion of small molecules from the outer compartment to the inner one (Fig. S7†). However, no obvious diffusion was observed between different compartments for the sequestrated macromolecules (Fig. S8†). The stability of the multi-compartment protocells was investigated by transmittance determination and the particle size measurements. There was no obvious difference in the transmittance of coacervate-in-coacervate after 24 h incubation (Fig. S9A†). The result was consistent with that of DLS (Fig. S9B†), which indicated that coacervate-in-coacervate structure was stable at least 24 h at room temperature.

Enzymatic cascade in compartmented coacervate microdroplets

Given that small molecules could diffuse between different compartments while macromolecules remained in their respective compartments, these properties allowed for the possibility of spatial immobilization of cascade enzymes as well as the implementation of incompatible reactions in compartmentalized coacervate systems. Here, GOx, HRP, and CAT were selected as model enzymes to perform spatially segregated cascade reactions. In the incompatible cascade reaction of GOx/HRP, the presence of CAT as a competitive enzyme consumed the intermediate of H_2O_2 and blocked the HRP-mediated peroxide reaction.

To confirm the spatially controlled immobilization of the cascade enzymes, GOx, HRP, and CAT were labeled with Cy5,

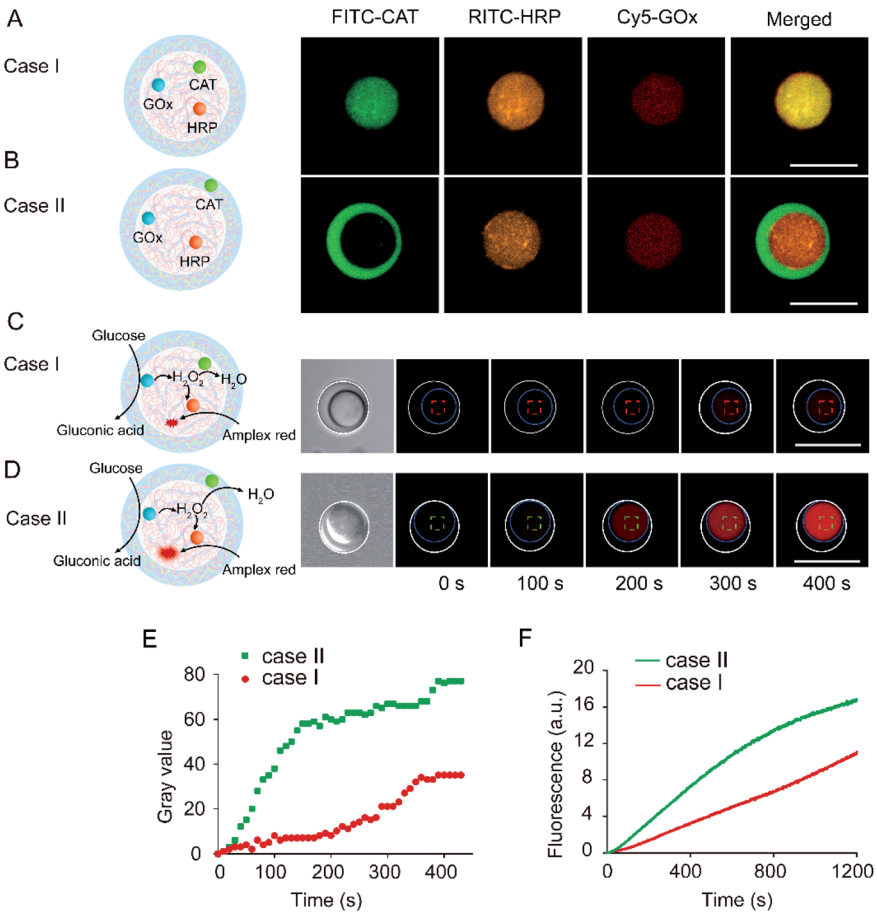

Fig. 5 Spatial organization of enzymatic cascade in a coacervate-in-coacervate multi-compartment. (A, B) Fluorescent imaging of multi-compartment protocells loaded with cascade enzymes in different compartments; GOx, HRP, and CAT were labeled with Cy5, RITC, and FITC, respectively. (C, D) Bright and time-dependent fluorescence images of compartmented protocells upon the addition of glucose (100 mM). Amplex Red (10 μM) was sequestered in the inner coacervates. Ex: 560 nm, Em: 585 nm. The inner and outer coacervates were outlined with dashed blue and white circles, respectively. Case I (A, C): GOx/HRP and CAT were all encapsulated in the inner coacervates. Case II (B, D): GOx/HRP and CAT were encapsulated in the inner and outer coacervates, respectively. (E) The time profile of the resorufin fluorescence change in the inner coacervate (Case I: red line, Case II: green line) shown in (C, D). (F) The time profile of the resorufin fluorescence oxidized from Amplex Red *via* cascade catalysis of GOx/HRP, obtained from the fluorometric determination of the coacervate supernatant.

rhodamine B isothiocyanate (RITC), and FITC, respectively, and then sequestrated into different coacervate phases during preparation. Especially, almost equivalent GOx and HRP were encapsulated in the coacervate-in-coacervate structure. The encapsulation efficiencies of CAT were determined as 98.6% and 98.2% in Case I and Case II, respectively (Table S2†). We speculated that the high encapsulation efficiency of the enzymes was due to the high partition coefficient and sequestration capability of coacervate. The enzymes' catalytic activities were investigated after encapsulation in different coacervate compartments. The enzymatic activity of GOx and HRP was determined through a 2,2′-azino-bis(3-ethylbenzothiazoline-6-sulfonic acid) colorimetric assay in the presence of various substrates in a buffer solution. The enzyme activity of GOx and HRP in PDDA/DNA coacervates (K_{cat} = 4830 s^{-1} for GOx, and 522 s^{-1} for HRP) was improved compared with that in the buffer solution (K_{cat} = 2680 s^{-1} for GOx, and 262 s^{-1} for HRP) (Table S3 and Fig. S10–S13†). This was attributed to the high sequestration of enzyme in the microdroplet interior. Similarly, the catalytic activities of CAT in the coacervates were also increased. However, some differences were observed between the turnover numbers of the PDDA/DNA (K_{cat} = 140 s^{-1}) and DEAE-dextran/CM-dextran (K_{cat} = 180 s^{-1}) coacervates (Fig. S14†). In Case I, green, red, and orange fluorescence could be observed in the inner coacervates, indicating the synchronous encapsulation of three enzymes in the same inner compartment (Fig. 5A). In Case II, green fluorescence occurred in the outer compartment, while a red/orange fluorescent signal occurred in the inner compartment, implying that GOx/HRP were encapsulated in the inner compartment and CAT in the outer compartment (Fig. 5B). The fluorescence observed in the compartments indicated that the three enzymes mostly encapsulated in the specified coacervate compartment due to the high sequestration capability of the coacervate matrix. The fluorescent probe of Amplex Red sequestrated in the inner coacervates was utilized to evaluate the spatially organized cascade reaction. No obvious fluorescence was observed in Case I. However, a remarkable fluorescence enhancement was seen in Case II, indicating the occurrence of a glucose-triggered GOx/HRP cascade reaction (Fig. 5C and D). A quantitative analysis of the single-microdroplet optical imaging showed that the fluorescence enhancement in Case II was 8.3 times faster than that in Case I within the first 150 s (Fig. 5E). Furthermore, compared with Case I, the results from the fluorometric determination of the coacervate supernatant also demonstrated an obvious fluorescence enhancement in Case II (Fig. 5F). Here, the differences were attributed to the distinct spatial organization of the cascade enzymes. In Case I, while the three enzymes were immobilized in the same coacervate phase, the HRP-mediated oxidation and CAT-mediated decomposition occurred in the same compartment. Due to high reaction rate of CAT, the CAT-mediated decomposition of H_2O_2 blocked the HRP-mediated Amplex Red oxidation and fluorescence generation. In Case II, while GOx/HRP and CAT were immobilized in separate phases, the HRP-mediated oxidation and CAT-mediated decomposition occurred in separate compartments. The HRP-mediated Amplex Red oxidation occupied a dominant role, leading to an efficient

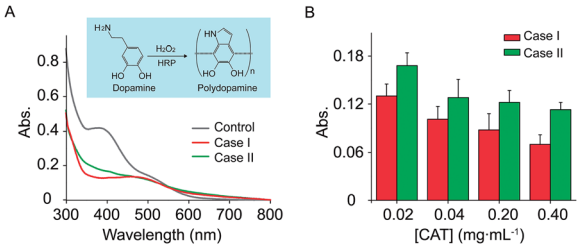

Fig. 6 (A) UV-vis absorption spectra of polydopamine in control (gray line), Case I (red line) and Case II (green line) after 10 min reaction, respectively. 0.22 μg mL^{-1} HRP and 0.18 μg mL^{-1} GOx encapsulated in inner compartment coacervate-in-coacervate structure, in the presence of 2.5 mM dopamine, 100 mM glucose. Control: GOx/HRP encapsulated in inner compartment, and without CAT. Case I: GOx/HRP and CAT encapsulated in inner compartment. Case II: GOx/HRP encapsulated in inner compartment, CAT in outer compartment. Inset: Chemical reaction of dopamine polymerization. (B) Absorption histogram of PDA in Case I (red line), Case II (green line) at different concentration of CAT (0.02–0.40 mg mL^{-1}) after 10 min reaction, respectively.

Amplex Red oxidation and a fast fluorescence enhancement. The immobilization of the cascade enzymes in different compartments led to a distinct reaction flux and product output. Therefore, based on the coacervate-in-coacervate multi-compartment protocell, the spatial position of the enzymatic cascade in different compartments facilitated the efficient occurrence of an incompatible reaction.

In our system, the different productions of H_2O_2 can be used for the modulation of dopamine polymerization. Polydopamine (PDA) is an emerging nature-inspired biopolymer material that possesses many interesting properties including self-assembly and universal adhesion.[47] Polydopamine was produced by HRP-catalyzed polymerization of dopamine in the presence of H_2O_2. Here, encapsulation of CAT in the inner coacervate (Case I) or outer coacervate (Case II) while GOx/HPR are immobilized in the inner, led to definitely different production of PDA. As showed in Fig. 6A, the polydopamine were successfully prepared in both Case I and Case II through enzymatic cascade reaction. More interestingly, the characterization adsorption of PDA at 410 nm in Case I was smaller than that of Case II. In order to investigate the effect of CAT on the synthesis of PDA, we changed the concentration of CAT to verify the production of PDA (Fig. 6B). Due to the consumption of the H_2O_2 by CAT, an increase of CAT led to a decrease of the PDA production. However, the adsorption of PDA in Case I was smaller than that of Case II, which was contributed to the different spatial organization of the cascade enzymes, and less leak of H_2O_2 in Case I.

Conclusions

In summary, in this research, a coacervate-in-coacervate microarchitecture was constructed as a multi-compartment protocell model, in which a spatially controlled competitive enzyme cascade was demonstrated. After CM-dextran and DEAE-dextran were deposited on the surface of as-prepared PDDA/DNA coacervates through layer-by-layer assembly, a high-level coacervate-in-coacervate microstructure was formed. The assembly

processes and resulting multi-compartment protocells were characterized through optical imaging and flow cytometry. The multi-compartment protocells were composed from two immiscible coacervate phases and demonstrated distinct physical and chemical properties, such as density, partition coefficient, and dielectric constant among others. In particular, the sequestrated small molecules allowed for diffusion between different coacervate compartments, though this was not applicable for macromolecules. We believe that the ability to construct a coacervate-in-coacervate structure through polyelectrolyte coacervation, layer-by-layer assembly, and molecular sequestration is a step forward in the bottom-up creation of synthetic protocells and opens up new avenues to a better understanding of the liquid–liquid separation phase and biomolecular condensates.

The multi-compartment architectures could serve as microreactors with cell-like sizes that mimic metabolic activities *via* cascade enzymatic reactions, and their permeability feature also provides a possibility for the construction of spatially segregated incompatible reactions. For example, GOx/HRP and CAT were respectively immobilized in the inner compartment and outer compartment, and three enzymes were all immobilized in the inner compartment. The fluorescence production rate of the glucose-mediated oxidation of Amplex Red in the former was 8.3 times larger than that of the latter. The different spatial organization of the enzymes and distinct reaction fluxes between the coacervate phases led to distinguishable signal generation and product outputs. In this system, biochemical reactions could be truly confined to provide increased efficacy, and incompatible reactions could be separated and, therefore, conducted simultaneously. Furthermore, the different productions of H_2O_2 in different cases were used for the modulation of dopamine polymerization. Thus, this concept of a multi-compartment coacervate structure could be extended to one-pot incompatible chemical reactions, resulting in an intelligent biomimetic soft system for bioproduction similar to that of nuclear body organelles or living cells.

Experimental

Chemicals and materials

Deoxyribonucleic acid (DNA, low molecular weight from salmon sperm), diethylaminoethyl-dextran (DEAE-dextran) hydrochloride powder (M_w: 50 w), polydiallyldimethyl ammonium chloride (PDDA) solution (average M_w 20 w to 35 w, 20.0% in weight), glucose, fluorescent probe Amplex Red and Hoechst 33258 were obtained from Sigma-Aldrich. 2,2′-Azino-bis(3-ethylbenzothiazoline-6-sulfonic acid) (ABTS), catalase (CAT), glucose oxidase (GOx), horseradish peroxidase (HRP), rhodamine B isothiocyanate (RITC) and carboxymethyl-dextran (CM-dextran) sodium salt were purchased from Sangon Biotech. Dopamine was obtained from J&K Scientific. All aqueous solutions of the experiments were used Milli-Q-purified water (18.2 MΩ cm).

Apparatus

Confocal laser scanning microscopic imaging (CLSM) was performed by TI-E+A1 SI, Nikon confocal laser scanning microscope with Ar laser. Adsorption spectra were performed on a UV-vis 2600 spectrophotometer (Shimadzu). Fluorescence spectra were recorded from F-7000 fluorescence spectrometer (Hitachi). Dynamic light scattering measurements and zeta potential measurements were performed by Nano Zetasizer analyzer (Malvern) with Dispersion Technology Software. Flow cytometer were conducted on Gallios Flow Cytometer (Beckman Coulter).

Preparation of PDDA/DNA coacervate microdroplets

The PDDA/DNA coacervate microdroplets were synthesized through electrostatic force by mixing of PDDA solution (10 mg mL^{-1}, pH = 8.0) and DNA solution (10 mg mL^{-1}, pH = 8.0) at different weight ratios (0.1–0.7). Typically, 0.5 mL of 10 mg mL^{-1} PDDA were mixed with 1.0 mL of 10 mg mL^{-1} DNA solution and after aging for 30 min, a suspension of positive charged PDDA/DNA coacervate microdroplets was obtained. Generally, the stock solution would be diluted up ([coacervate] = 1 mg mL^{-1}) for further use.

Preparation of PDDA/DNA@CM-dextran/DEAE-dextran microdroplets

PDDA/DNA@CM-dextran/DEAE-dextran microdroplets with coacervate-in-coacervate structure were prepared through three successive steps. Step 1, mixture of PDDA solution (10 mg mL^{-1}, pH = 8.0) and DNA solution (10 mg mL^{-1}, pH = 8.0) in a weight ratio of 0.6 resulted in the formation of positively charged PDDA/DNA coacervate microdroplets. Secondly, 0.3 mL CM-dextran solution (10 mg mL^{-1}, pH = 8.0) was added into 0.1 mL preformed PDDA/DNA coacervate suspension, which reversed the zeta potential of coacervates from positive to negative. Finally, 0.12 mL DEAE-dextran solution (10 mg mL^{-1}, pH = 8.0) was added and incubated for 10 min, which led to the formation of PDDA/DNA@CM-dextran/DEAE-dextran coacervate microdroplets. Especially, the coacervate-in-coacervate was diluted up to ten times ([coacervate] = 1 mg mL^{-1}) for dynamic light scattering and zeta potential measurements. In addition, the turbidity experiment, Amplex Red fluorescence assay, enzymatic activity measurements, confocal laser scanning microscopy assay and flow cytometry assays were all used 1 mg mL^{-1} coacervate-in-coacervate suspension.

Amplex Red fluorescence assay

0.16 μg mL^{-1} GOx, 0.22 μg mL^{-1} HRP and 10 μM Amplex Red were loaded in the different compartments of the preformed coacervate-in-coacervate microdroplets (5 mg mL^{-1}) through synchronous assembly. To elicit the cascade reaction, 100 mM glucose was added into the coacervate suspension and the fluorescent kinetics of Amplex Red was determined through fluorescence spectrometer with excitation and emission at 561 nm and 585 nm, respectively.

Enzymatic activity measurements

The enzymatic activity of GOx and HRP were evaluated following H_2O_2–ABTS colorimetric assay. To evaluate the enzymatic activity

of GOx in coacervate, GOx (0.08 μg mL^{-1}), HRP (0.22 μg mL^{-1}), ABTS (2.0 mM) were loaded in coacervate compartment, then a time-dependent UV absorption change of oxidation product (ABTS-diradical) at 418 nm (ε_{418} = 36 800 M^{-1} cm^{-1}) in coacervate was recorded in the presence of different amounts of glucose (1–400 mM). Especially, the coacervate was removed by centrifugation at 6000 rpm for 10 min to eliminate the inherent absorption of coacervate-in-coacervate structure. All the H_2O_2–ABTS colorimetric assay used the supernatant and repeated three times at least in this work.

To evaluate the enzyme activity of HRP in coacervate microdroplets, HRP (0.022 μg mL^{-1}) and ABTS (2.0 mM) were loaded in coacervate compartment, then a time-dependent UV absorption change of oxidation product (ABTS-diradical) at 418 nm (ε_{418} = 36 800 M^{-1} cm^{-1}) in coacervate was recorded in the presence of different amounts of H_2O_2 (5–1000 μM).

To evaluate the enzyme activity of CAT in different coacervate compartment, time dependent absorbance change of H_2O_2 at 240 nm was examined in the concentration of H_2O_2 (2.5 mM).

Determination of protein loading in coacervate structure

The sequestration of GOx-HRP/CAT into the coacervate-in-coacervate droplets was determined using partition constant (K) assays that were carried out on the equilibrium aqueous solution phases isolated by centrifugation from a mixture containing coacervate-in-coacervate, GOx-HRP/CAT. CAT, GOx/HRP labelled with fluorescein isothiocyanate (FITC), rhodamine-B-isothiocyanate (RITC), respectively. The concentration of GOx-HRP/CAT in the external aqueous phase ($[enzyme]_{out}$) was determined from absorbance and the volume of the continuous phase (V_{out}). Given the total number of units of enzyme was added to the system ($[enzyme]_{total}V_{total}$), K was determined from the relationships: $K = [enzyme]_{in}/[enzyme]_{out}$, and $[enzyme]_{in} = ([enzyme]_{total}V_{total} - [enzyme]_{out}V_{out})/V_{in}$, where $[enzyme]_{in}$ and V_{in} are the concentration of enzyme in the coacervate microdroplet and the total volume of the coacervate phase.

In this experiment, 0.16 μg mL^{-1} RITC–GOx, 0.22 μg mL^{-1} RITC–HRP and 0.018 mg mL^{-1} FITC–CAT were added into coacervate-in-coacervate suspension of Case I or Case II, respectively. Supernatant and coacervate phase were determined using the different absorbance of dyes (FITC, RITC) by centrifugation at 6000 rpm for 10 min to eliminate the inherent absorption of coacervate-in-coacervate structure.

Enzymatic synthesis of polydopamine

The dopamine polymerization was conducted as follows. 2.5 mM dopamine and 100 mM glucose in 0.1 mL 50 mM PBS were added into 0.1 mL coacervate microdroplet suspension. After reaction for 10 min, the UV-vis spectra were determined. In order to explore the effect of CAT, we determined the absorption spectrum of polydopamine by increasing the concentration of CAT (0.02–0.40 mg mL^{-1}) in Case I, and Case II, respectively. The HRP-based enzymatic reaction was initiated by enzymatic reaction of glucose oxidase producing H_2O_2 for stirred for 10 min.

Confocal laser scanning microscopy imaging

Confocal microscopy imaging was performed using a Nikon confocal laser scanning microscope. Coacervate microdroplets loaded with Hoechst 33258, FITC–CAT, RITC–HRP, and Cy5–GOx were imaged with under excitation by 405, 488, 560, and 630 nm laser, respectively. Confocal three-dimensional imaging was conducted through Z-scanning and the three-dimensional reconstitution was performed by Image J software.

Flow cytometry assays

During the preparation of compartmented coacervate microdroplets, different types of coacervates (PDDA/DNA, PDDA/DNA@CM-dextran, and PDDA/DNA@CM-dextran/DEAE-dextran) were analyzed by a flow cytometer (Gallios, Beckman Coulter). Prior to flow cytometry, all the compartmented coacervates were diluted up to ten times without destabilization of the droplets. For each microdroplets, 10 000 events were counted, and two-dimensional (2D) dot plots of forward light scattered height (FSC-H) *versus* side light scattered height (SSC-H) were recorded.

Conflicts of interest

There are no conflicts to declare.

Acknowledgements

The authors gratefully acknowledge the financial support of the Natural Science Foundation of China (21735002, 21575037, 21778016, 21675046, and 21877030).

References

1 S. Koga, D. S. Williams, A. W. Perriman and S. Mann, *Nat. Chem.*, 2011, **3**, 720–724.
2 B. C. Buddingh' and J. C. M. van Hest, *Acc. Chem. Res.*, 2017, **50**, 769–777.
3 J. C. Fu and J. B. Schlenoff, *J. Am. Chem. Soc.*, 2016, **138**, 980–990.
4 J. P. Douliez, N. Martin, C. Gaillard, T. Beneyton, J. C. Baret, S. Mann and L. Beven, *Angew. Chem., Int. Ed.*, 2017, **56**, 13689–13693.
5 B. Drobot, J. M. Iglesias-Artola, K. Le Vay, V. Mayr, M. Kar, M. Kreysing, H. Mutschler and T. D. Tang, *Nat. Commun.*, 2018, **9**, 3643.
6 T. D. Tang, D. van Swaay, A. deMello, J. L. R. Anderson and S. Mann, *Chem. Commun.*, 2015, **51**, 11429–11432.
7 E. Sokolova, E. Spruijt, M. M. K. Hansen, E. Dubuc, J. Groen, V. Chokkalingam, A. Piruska, H. A. Heus and W. T. S. Huck, *Proc. Natl. Acad. Sci. U. S. A.*, 2013, **110**, 11692–11697.
8 A. F. Mason, B. C. Buddingh', D. S. Williams and J. C. M. van Hest, *J. Am. Chem. Soc.*, 2017, **139**, 17309–17312.
9 C. P. Brangwynne, C. R. Eckmann, D. S. Courson, A. Rybarska, C. Hoege, J. Gharakhani, F. Jülicher and A. A. Hyman, *Science*, 2009, **324**, 1729–1732.

10 S. Jain, J. R. Wheeler, R. W. Walters, A. Agrawal, A. Barsic and R. Parker, *Cell*, 2016, **164**, 487–498.
11 A. Zimbera, Q. D. Nguyenb and C. Gespach, *Cell. Signalling*, 2004, **16**, 1085–1104.
12 W. M. Aumiller Jr and C. D. Keating, *Nat. Chem.*, 2016, **8**, 129–137.
13 M. Bayoumi, H. Bayley, G. Maglia and K. T. Sapra, *Sci. Rep.*, 2017, **7**, 45167.
14 X. L. Liu, P. Formanek, B. Voit and D. Appelhans, *Angew. Chem., Int. Ed.*, 2017, **56**, 16233–16238.
15 R. Chandrawati, M. P. van Koeverden, H. Lomas and F. Caruso, *J. Phys. Chem. Lett.*, 2011, **2**, 2639–2649.
16 Y. Elani, R. V. Law and O. Ces, *Nat. Commun.*, 2014, **5**, 5305.
17 M. S. Long, C. D. Jones, M. R. Helfrich, L. K. Mangeney-Slavin and C. D. Keating, *Proc. Natl. Acad. Sci. U. S. A.*, 2005, **102**, 5920–5925.
18 M. Marguet, C. Bonduelle and S. Lecommandoux, *Chem. Soc. Rev.*, 2012, **42**, 512–529.
19 C. Love, J. Steinkühler, D. T. Gonzales, N. Yandrapalli, T. Robinson, R. Dimova and T.-Y. D. Tang, *Angew. Chem., Int. Ed.*, 2020, **59**, 5950–5957.
20 A. X. Lu, H. Oh, J. L. Terrell, W. E. Bentley and S. R. Raghavan, *Chem. Sci.*, 2017, **8**, 6893–6903.
21 A. Belluati, S. Thamboo, A. Najer, V. Maffeis, C. von Planta, I. Craciun, C. G. Palivan and W. Meier, *Adv. Funct. Mater.*, 2020, DOI: 10.1002/adfm.202002949.
22 C. M. Paleos, D. Tsiourvas, Z. Sideratou and A. Pantos, *J. Controlled Release*, 2013, **170**, 141–152.
23 E. Rideau, R. Dimova, P. Schwille, F. R. Wurm and K. Landfester, *Chem. Soc. Rev.*, 2018, **47**, 8572–8610.
24 C. Lopresti, H. Lomas, M. Massignani, T. Smart and G. Battaglia, *J. Mater. Chem.*, 2009, **19**, 3576–3590.
25 D. Mertz, J. W. Cui, Y. Yan, G. Devlin, C. Chaubaroux, A. Dochter, R. Alles, P. Lavalle, J. C. Voegel, A. Blencowe, P. Auffinger and F. Caruso, *ACS Nano*, 2012, **6**, 7584–7594.
26 Y. Qiao, M. Li, R. Booth and S. Mann, *Nat. Chem.*, 2017, **9**, 110–119.
27 D. Garenne, L. Beven, L. Navailles, F. Nallet, E. J. Dufourc and J. P. Douliez, *Angew. Chem., Int. Ed.*, 2016, **55**, 13475–13479.
28 S. B. Li, X. J. Wang, W. Mu and X. J. Han, *Anal. Chem.*, 2019, **91**, 6859–6864.
29 B. Wong, C. Boyer, C. Steinbeck, D. Peters, J. Schmidt, R. van Zanten, B. Chmelka and J. A. Zasadzinski, *Adv. Mater.*, 2011, **23**, 2320–2325.
30 N. N. Deng, M. A. Vibhute, L. F. Zheng, H. Zhao, M. Yelleswarapu and W. T. S. Huck, *J. Am. Chem. Soc.*, 2018, **140**, 7399–7402.
31 B. Städler, R. Chandrawati, K. Goldie and F. Caruso, *Langmuir*, 2009, **25**, 6725–6732.
32 X. Huang and B. Voit, *Polym. Chem.*, 2013, **4**, 435–443.
33 B. Städler, R. Chandrawati, A. D. Price, S. F. Chong, K. Breheney, A. Postma, L. A. Connal, A. N. Zelikin and F. Caruso, *Angew. Chem., Int. Ed.*, 2009, **48**, 4359–4362.
34 J. W. Maina, J. J. Richardson, R. Chandrawati, K. Kempe, M. P. van Koeverden and F. Caruso, *Langmuir*, 2015, **31**, 7776–7781.
35 R. J. R. W. Peters, M. Marguet, S. Marais, M. W. Fraaije, J. C. M. van Hest and S. Lecommandoux, *Angew. Chem., Int. Ed.*, 2014, **53**, 150–154.
36 M. Marguet, L. Edembe and S. Lecommandoux, *Angew. Chem., Int. Ed.*, 2012, **51**, 1173–1176.
37 J. W. Hindley, Y. Elani, C. M. McGilvery, S. Ali, C. L. Bevan, R. V. Law and O. Ces, *Nat. Commun.*, 2018, **9**, 1093.
38 H. L. Tan, S. Guo, N. D. Dinh, R. Luo, L. Jin and C. H. Chen, *Nat. Commun.*, 2017, **8**, 663.
39 S. Deshpand, F. Brandenburg, A. Lau, M. G. F. Last, W. K. Spoelstra, L. Reese, S. Wunnava, M. Dogterom and C. Dekker, *Nat. Commun.*, 2019, **10**, 1800.
40 R. Booth, Y. Qiao, M. Li and S. Mann, *Angew. Chem., Int. Ed.*, 2019, **58**, 9120–9124.
41 N. N. Deng and W. T. S. Huck, *Angew. Chem., Int. Ed.*, 2017, **56**, 9736–9740.
42 M. G. F. Last, S. Deshpande and C. Dekker, *ACS Nano*, 2020, **14**, 4487–4498.
43 A. F. Mason, N. A. Yewdall, P. L. W. Welzen, J. X. Shao, M. van Stevendaal, J. C. M. van Hest, D. S. Williams and L. K. E. A. Abdelmohsen, *ACS Cent. Sci.*, 2019, **5**, 1360–1365.
44 N. Martin, J. P. Douliez, Y. Qiao, R. Booth, M. Li and S. Mann, *Nat. Commun.*, 2018, **9**, 3652.
45 F. M. Boisvert, S. van Koningsbruggen, J. Navascués and A. I. Lamond, *Nat. Rev. Mol. Cell Biol.*, 2007, **8**, 574–585.
46 A. C. Romano, E. M. Espana, S. H. Yoo, M. T. Budak, J. M. Wolosin and S. C. G. Tseng, *Invest. Ophthalmol. Visual Sci.*, 2003, **44**, 5125–5129.
47 M. Z. Dai, T. Huang, L. Chao, Q. J. Xie, Y. M. Tan, C. Chen and W. H. Meng, *Talanta*, 2016, **149**, 117–123.